AIAA Propulsion and Energy Forum
19-22 August 2019, Indianapolis, IN
AIAA Propulsion and Energy 2019 Forum

10.2514/6.2019-3987

Erosion of a meshed reflector in the plume of a Hall effect thruster, Part 1: Modeling

Mackenzie E. Meyer*, Matthew P. Byrne†, Benjamin A. Jorns‡, and Iain D. Boyd§
University of Michigan, Ann Arbor, Michigan, 48109

A model for the erosion of a meshed reflector by sputtering in the plume of a Hall effect thruster is presented, and results are compared to experimental measurements. The ion current density and ion energy distribution function at the location of the meshed reflector are required to determine the erosion. These properties are obtained through both numerical simulation and experimental measurements. The sputter yield as a function of energy and angle of incidence is also required to determine the erosion, and this work considers several models. The erosion is then modeled by discretizing the cross section of a single wire in the meshed reflector and modeling how each discretized surface erodes over time. The results of the model using different sputter yield models are compared to experimental measurements of the eroded wire profiles to assess and verify the model. The average of these results using different sputter yield models accurately predicts the experimentally measured eroded wire profiles to within 35% of the wire radius at different locations in the plume. With this verified model, the erosion of meshed reflectors in the plume of other electric propulsion devices can be determined.

Nomenclature

$\vec{F}$	=	Force, N
q	=	Ion charge, C
m_s	=	Atomic mass of species s, kg
$\vec{E}$	=	Electric field, V/m
ϕ	=	Plasma potential, V
T_s	=	Temperature of species s, K
n_s	=	Number density of species s, m^{-3}
$\vec{v}_s$	=	Velocity of species s, m/s
C_i	=	Ionization rate, m^3/s
e	=	Fundamental charge, 1.6×10^{-19} C
p_s	=	Pressure of species s, Pa
σ	=	Classical electrical conductivity, $(\Omega \text{m})^{-1}$
$\vec{J}_s$	=	Current density of species s, A/m^3
k	=	Boltzmann constant, 1.38×10^{-23} J/K
κ_s	=	Thermal conductivity of species s, W/(Km)
ν_s	=	Total collision frequency of species s, s^{-1}
ν_{es}	=	Collision frequency of electrons and species s, s^{-1}
σ_r	=	Reference cross section, $\sigma_r = 5 \times 10^{-20}$ m^2
c_s	=	Mean thermal speed of species s, m/s
ε_i	=	Ionization energy of xenon, 12.7 eV
ψ	=	Stream function
E	=	Ion energy, eV
θ	=	Incident angle, degrees

*Ph.D. Pre-Candidate, Applied Physics, AIAA Student Member.
†Ph.D. Candidate, Applied Physics, AIAA Student Member.
‡Assistant Professor, Department of Aerospace Engineering, AIAA Senior Member.
§James E. Knott Professor, Department of Aerospace Engineering, AIAA Fellow.

ϵ	=	Reduced energy
E_{th}	=	Threshold energy, eV
$s_n(\epsilon)$	=	Nuclear stopping cross section
$Y(E)$	=	Normal incidence sputter yield, atoms sputtered/incident ion
Q	=	Fit parameter for the Bohdansky formula
a, b	=	Fit parameters for the Ikuse normal incidence model
Q, μ, λ	=	Fit parameters for the Eckstein normal incidence model
$Y(E, \theta)$	=	Angular incidence sputter yield, atoms sputtered/incident ion
$f, \theta_{opt}, f_{sig}, p$	=	Fit parameters for the Yamamura angular incidence model
a, α, β	=	Fit parameters for Wei angular incidence model
Δx	=	Erosion depth, m
j_i	=	Ion current density, A/m^2
ρ_s	=	Density of species s, kg/m^3
Δt	=	Time exposed to the plume, s
$f(E_i)$	=	Discrete ion energy distribution function
(x, y)	=	Endpoints in the erosion model
dt	=	Time step, s
Subscripts	=	
e	=	Electrons
i	=	Ions
n	=	Neutral atoms
H	=	Heavy species
m	=	Target material

I. Introduction

Electric propulsion (EP) devices, including Hall effect thrusters, are being used increasingly on Earth-orbiting satellites and for deep-space missions. While these devices offer a high specific impulse compared to chemical propulsion systems, there is a risk of causing damage to the spacecraft components. Since these low thrust devices need to operate for long periods of time, their highly energetic propellant can lead to ion impact erosion of key spacecraft components[1]. Understanding how material erodes in the plume of an EP device is therefore a critical aspect of integrating these devices onto a spacecraft. One example of a spacecraft component that is particularly critical for commercial systems is the meshed reflector. Meshed reflectors are parts of antenna used on satellites and can lose functionality after a certain level of erosion. Erosion of this level can offset the gains in specific impulse and lifetime afforded by the EP device.

Since the meshed reflectors are typically made of a mesh of molybdenum wires coated with gold, the erosion of wires due to sputtering by the ions in the plume of an EP device needs to be understood. While the erosion of a planar surface in the plume of a Hall effect thruster has been previously investigated[2–4], the erosion of a cylindrical surface in these conditions has not been studied. The goal of this two part work is to examine the modeling of the erosion of a meshed reflector in the plume of a Hall effect thruster. In this part, the development of an erosion model for the meshed reflectors is detailed. This model considers the erosion of a single wire, as each wire in the meshed reflector will erode in the same manner. In the second part of this work[5], the experimental setup is described. The results of the experimental testing include the plume properties and eroded wire profiles at different locations in the plume. The wire profiles are used to verify the results of the erosion model calculated using the experimentally measured plume properties.

This paper is organized as follows. First, the methods of modeling the plume, sputter yield, and wire erosion are discussed. Results of the plume modeling and wire erosion modeling are then presented, and those results are compared to the corresponding experimental measurements. The implications of these results for spacecraft, as well as the limitations of the erosion model, are discussed.

II. Modeling

Several key components are necessary for evaluating the erosion of a wire. Plume properties such as the ion current density and ion energy distribution function (IEDF) at the surface of the wire are required. These properties are obtained through a plume simulation. The sputter yield, or atoms emitted from the surface per incident ion, is determined using the IEDF. With the sputter yield and the ion current density, the erosion of a wire can be modeled by discretizing the cross section of the wire into small, planar surfaces and calculating how those surfaces erode over time.

This section first presents the plume simulation that provides ion current density and IEDF. The sputter yield models are then presented. Finally, the model of the erosion of a wire is discussed.

A. Plume Modeling

The ion current density and IEDF are required to determine the erosion of a wire. While experimental measurements give the best estimates of these quantities, high fidelity numerical simulations enable the prediction of erosion in the plume of other EP devices by estimating the required plume properties. This section describes one such high fidelity model.

Plume properties such as the ion current density and IEDF vary at different locations in the plume. The xenon ions accelerated by the axial electric field in a Hall effect thruster form a high density beam of energetic ions that diverges about 30° from the thruster centerline. At larger angles from the thruster centerline, charge-exchange (CEX) collisions dominate. These collisions occur when an electron is transferred from a neutral xenon atom to an energetic ion, resulting in a slow-moving ion and a fast-moving neutral atom. These slow-moving ions are less energetic than the ions in the beam, and the density of ions at large angles from the thruster centerline is lower than the density of ions in the beam.

The ion current density and IEDF can be determined by the 2D axisymmetric simulation MONACO-PIC (MPIC). This steady state simulation uses the particle-in-cell (PIC) and direct simulation Monte Carlo (DSMC) methods to model the ion and neutral atom motion and describes the electrons by the three fluid conservation equations. The simulation uses macroparticles to represent a large number of ions and neutral atoms. Both momentum exchange (MEX) and CEX collisions between the ions and neutral atoms are considered. The DSMC method performs the collisions of the macroparticles by randomly selecting pairs of macroparticles to collide in a given cell. This method conserves both momentum and energy. The five types of collisions considered are neutral atom and neutral atom MEX, neutral atom and singly charged ion MEX and CEX, and neutral atom and doubly charged ion MEX and CEX. The effects of background pressure are included by introducing neutral atoms in each cell that collide with other particles but do not move themselves. The PIC method moves the ions according to the force $\vec{F}$ from the local electric field $\vec{E}$

$$\vec{F} = q\vec{E} \tag{1}$$

New macroparticles are injected into the simulation at the inlet boundary. The velocity of these macroparticles is determined from a drifting Maxwell-Boltzmann velocity distribution function with specified drift velocity and specified temperatures in each direction. In this work, the inlet boundary is an effective inlet along a magnetic field line in the near-field plume, as described in [6].

Since the electrons adjust to the local electric field faster than the ions due to the mass of electrons being much smaller than that of the ions, the electrons can be described using a detailed fluid model, as documented in [6, 7]. Assuming quasineutrality, the electron number density n_e is determined by the ion number density. This detailed fluid model solves for the plasma potential ϕ, electron temperature T_e, and electron velocity $\vec{v_e}$ using the electron continuity equation (Eq. 2), the electron momentum equation (Eq. 3), and the electron energy equation (Eq. 4)

$$\frac{\partial}{\partial t} n_e + \nabla \cdot (n_e \vec{v_e}) = n_e n_a C_i \tag{2}$$

$$\frac{\partial}{\partial t}\left(m_e n_e \vec{v_e}\right) + m_e n_e (\vec{v_e} \cdot \nabla)\vec{v_e} = -e n_e \vec{E} - \nabla p_e + \frac{e n_e}{\sigma}\vec{J_e} \tag{3}$$

$$\frac{\partial}{\partial t}\left(\frac{3}{2} n_e k T_e\right) + \frac{3}{2} n_e (\vec{v_e} \cdot \nabla) k T_e + p_e \nabla \cdot \vec{v_e} = \nabla \cdot \kappa_e \nabla T_e + 3(\vec{J_e} \cdot \vec{E})\frac{m_e}{m_i} \nu_e n_e k (T_e - T_H) - n_e n_a C_i \varepsilon_i \tag{4}$$

The electron pressure is $p_e = n_e k T_e$. The classical electrical conductivity σ is

$$\sigma = \frac{e^2 n_e}{m_e \nu_e} \tag{5}$$

and the electron thermal conductivity κ_e is

$$\kappa_e = \frac{2.4}{1 + \frac{\nu_{ei}}{\sqrt{2}\nu_e}} \frac{k^2 n_e T_e}{m_e \nu_e} \tag{6}$$

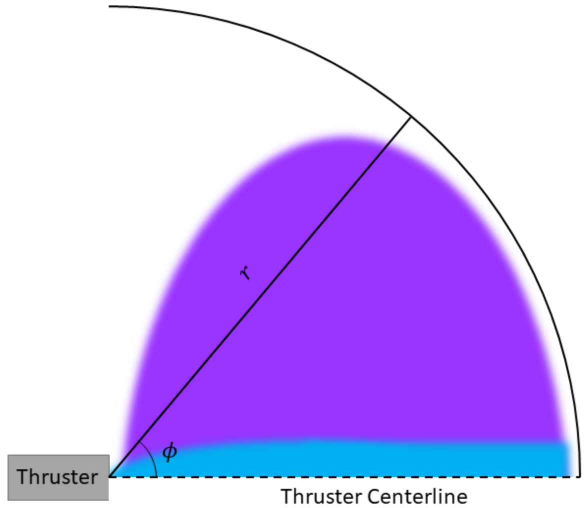

Fig. 1 Location on an arc of distance r and angle from the thruster centerline ϕ.

The total electron collision frequency ν_e is the sum of the ion-electron collision frequency ν_{ei} and the neutral-electron collision frequency ν_{en}. The ionization rate C_i is taken from [8]

$$C_i = \sigma_r c_e \left(1 + \frac{T_e \varepsilon_i}{(T_e + \varepsilon_i)^2}\right) \exp\left(-\frac{\varepsilon_i}{T_e}\right) \tag{7}$$

where T_e is expressed in eV.

In steady state, all of the time derivatives in the fluid equations are neglected. The electron continuity equation, in terms of the stream function $\nabla\psi = n_e \vec{v}_e$, can be rewritten as

$$\nabla^2 \psi = n_e n_a C_i \tag{8}$$

The electron momentum equation can be represented as a generalized Ohm's law

$$\vec{J}_e = \sigma\left[-\nabla\phi + \frac{1}{e n_e}\nabla(n_e k T_e)\right] \tag{9}$$

By applying charge continuity in steady state ($\nabla \cdot \vec{J}_e = 0$), this equation can be solved for ϕ. The electron energy equation can be solved for the T_e

$$\nabla^2 T_e = -\nabla \log \kappa_e \cdot \nabla T_e + \frac{1}{\kappa_e}\left(-\vec{J}_e \cdot \vec{E} + \frac{3}{2} n_e (\vec{v}_e \cdot \nabla) k T_e + p_e \nabla \cdot \vec{v}_e + \frac{3 m_e}{m_i} \nu_e n_e k (T_e - T_H) + n_e n_a C_i \varepsilon_i\right) \tag{10}$$

With the plasma potential calculated from the above equations, the local electric field $\vec{E} = -\nabla\phi$ can be derived and used to calculate the motion of the ions. Further details about MPIC can be found in [6].

The results of MPIC include the ion current density and IEDFs along an arc of specified distance from the thruster at various angles from the thruster centerline, as illustrated in Fig. 1. These plume properties are necessary to determine the erosion of a wire.

B. Sputter Modeling

The sputter yield is required to determine the erosion of a surface. The angular incidence sputter yield depends on the ion energy E and the incident angle θ of the ions with respect to the surface normal as illustrated in Fig. 2. The sputter yield also depends on the target material and the incident ion species. Since the wires of the meshed reflector are composed of both molybdenum and gold, the sputter yields of both materials by xenon ions are considered. The angular incidence sputter yield can be separated into two parts: the normal incidence sputter yield $Y(E)$ that relies on the ion energy and an angular factor that relies on the angle of incidence.

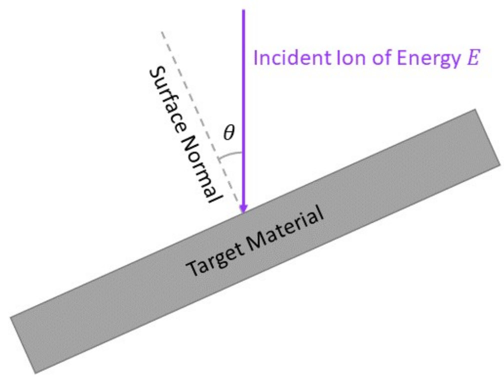

Fig. 2 Geometry of sputtering.

1. Normal Incidence Sputter Yield

In this work, three different normal incidence sputter yield models are considered for sputtering of gold and molybdenum. All of these normal incidence sputter yield models depend on a threshold energy E_{th}, and sputtering only occurs when the incident ion energy is above this threshold. One of the the normal incidence sputter yield models considered for molybdenum sputtering is the Bohdansky formula. This model uses the nuclear stopping cross section $s_n(\epsilon)$ based on the Krypton-Carbon potential to determine the sputter yield[9, 10]

$$s_n(\epsilon) = \frac{0.5\log(1 + 1.2288\epsilon)}{\epsilon + 0.1728\sqrt{\epsilon} + 0.008\epsilon^{0.1504}} \tag{11}$$

$$Y(E) = Q s_n(\epsilon)\left(1 - \left(\frac{E_{th}}{E}\right)^{2/3}\right)\left(1 - \frac{E_{th}}{E}\right)^2 \tag{12}$$

Here, ϵ is the reduced energy. The fit parameter $Q = 23.1$ and the threshold energy $E_{th} = 39.3$ eV are given by Tartz in [11]. A normal incidence sputter yield model for gold sputtering is given by Ikuse

$$Y(E) = a\left(1 - \sqrt{\frac{E_{th}}{E}}\right)^{5/2}\left[1 + b\left(\sqrt{\frac{E}{E_{th}}} - 1\right)\right] \tag{13}$$

with fit parameters $a = 0.37847$ and $b = 5.35641$. The threshold energy is $E_{th} = 28.5528$ eV[12]. The normal incidence sputter yield model proposed by Eckstein is used for both gold and molybdenum sputtering

$$Y(E) = Q s_n(\epsilon)\frac{\left(\frac{E}{E_{th}} - 1\right)^{\mu}}{\frac{\lambda}{w} + \left(\frac{E}{E_{th}} - 1\right)^{\mu}} \tag{14}$$

where $s_n(\epsilon)$ is the nuclear stopping cross section as in equation 11, $w = \epsilon + 0.1728\sqrt{\epsilon} + 0.008\epsilon^{0.1504}$, and ϵ is the reduced energy[13]. The fit parameters Q, λ, and μ and the threshold energy E_{th} are given by Yim for both gold and molybdenum in [3].

These three normal incidence models are compared in Fig. 3 for typical ion energies in a Hall effect thruster plume, with the Eckstein normal incidence model shown in the figure for both gold and molybdenum. At very low energies, the normal incidence sputter yield varies rapidly with energy. At high energies, the normal incidence sputter yield does not vary as quickly with energy. Additionally, the normal incidence sputter yield of molybdenum is lower than the normal incidence sputter yield of gold. A gold surface will therefore emit more atoms than a molybdenum surface per incident ion.

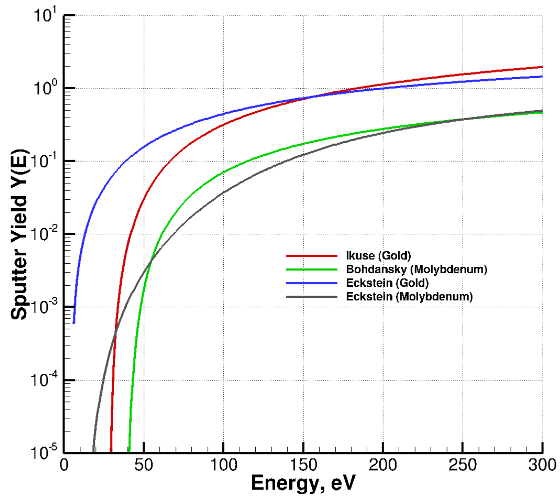

Fig. 3 Normal incidence sputter yield.

2. Angular Incidence Sputter Yield

Two angular incidence sputter yield models that can be applied to both gold and molybdenum are considered in this work. The first angular incidence sputter yield model follows the work of Yamamura in [14]

$$Y(E,\theta) = Y(E)\Big(\frac{1}{\cos\theta}\Big)^f \exp\left(-f\cos\theta_{opt}\Big(\frac{1}{\cos\theta}-1\Big)\right) \tag{15}$$

where f and θ_{opt} are fit parameters. $f = 6.8$ and $\theta_{opt} = 49.0°$ for a gold surface[2]. For a molybdenum surface, f and θ_{opt} depend on the energy of the incident ion

$$f = f_{sig}\left(1 + 2.5\frac{\sqrt{\frac{E_{th}}{E}}}{1-\sqrt{\frac{E_{th}}{E}}}\right) \tag{16}$$

$$\theta_{opt} = 90° - 286.0\Big(\frac{p}{\sqrt{E}}\Big)^{0.45} \tag{17}$$

where $f_{sig} = 2.1$ and $p = 0.15$[11]. E_{th} is the threshold energy given by the normal incidence sputter yield model. The second angular incidence sputter yield model considered is from the work of Wei in [15]

$$Y(E,\theta) = Y(E)\frac{\alpha}{A}\cos\theta\exp\left(\frac{a^2}{2\alpha^2}\Big[1-\frac{\alpha^2}{A^2}\cos^2\theta\Big]\right) \tag{18}$$

where $A^2 = \alpha^2\cos^2\theta + \beta^2\sin^2\theta$ and a, α, and β are fit parameters. This equation can be rewritten as

$$Y(E,\theta) = Y(E)\frac{1}{\sqrt{1+(\beta/\alpha)^2\tan^2\theta}}\exp\left(\frac{1}{2}\Big(\frac{a}{\alpha}\Big)^2\Big[1-\frac{1}{1+(\beta/\alpha)^2\tan^2\theta}\Big]\right) \tag{19}$$

where $\frac{a}{\alpha}$ and $\frac{\beta}{\alpha}$ are now considered fit parameters with values for gold and molybdenum given in [3].

Fig. 4 compares $Y(E,\theta)/Y(E)$ for the two models discussed. For all angular incidence sputter yield models shown in Fig. 4, the maximum sputter yield is not at normal incidence (0°). Rather, it is at some optimal angle between 30° and 60°. At large angles of incidence beyond the optimal angle, the Yamamura angular incidence model predicts a rapid decrease of the sputter yield towards 0, while the Wei angular incidence model predicts a smoother decrease. In Fig. 4a,

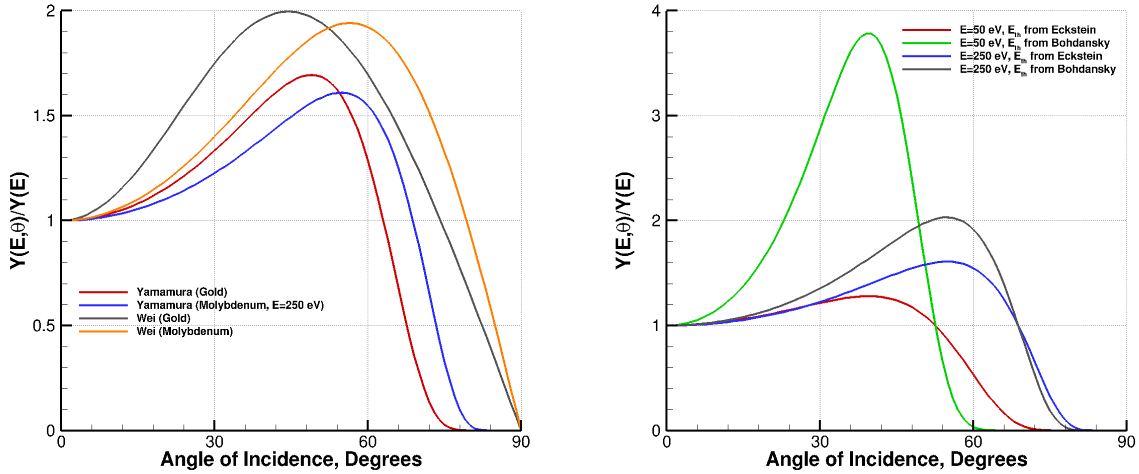

(a) Yamamura and Wei angular incidence sputter yield models. **(b) Yamamura angular incidence model for molybdenum.**

Fig. 4 Angular incidence sputter yield.

the Yamamura angular incidence model was calculated with an ion energy of 250 eV and the threshold energy from the Eckstein normal incidence model. To illustrate the dependence of the fit parameters of the Yamamura angular incidence model for molybdenum on energy and threshold energy, profiles at two different ion energies and the threshold energies of the Bohdansky formula and Eckstein normal incidence model are shown Fig. 4b. The optimal angle is lower with an ion energy of 50 eV than 250 eV. At 50 eV, the Yamamura angular incidence model with the threshold energy of the Bohdansky formula predicts almost four times as much sputtering as the model with the threshold energy of the Eckstein normal incidence model does because the threshold energy of the Bohdansky formula is much closer to 50 eV. At 250 eV, the Yamamura angular incidence model with the threshold energy of the Bohdansky formula decreases to zero faster than the threshold energy of the Eckstein normal incidence model. These angular incidence sputter yield models were chosen due to the availability of fit parameters for both gold and molybdenum at energies typical of a Hall effect thruster plume[3, 11]. Additionally, the differing values of the sputter yield at large angles of incidence influence the results of the erosion model.

Many uncertainties surround the sputter yield models. The experimental measurements of the sputter yield are influenced by a variety of factors, including surface roughness and non-monoenergetic ion beams[3]. Since the fit parameters of the sputter yield models are determined from the experimental measurements, the values of the fit parameters have an associated uncertainty.

C. Wire Erosion Modeling

The erosion of a surface at a given location in the plume of an EP device can be determined using the plume properties and the angular incidence sputter yield described in the previous two sections. The equation for the erosion depth of a flat surface is

$$\Delta x = \frac{j_i}{q}\frac{m_m}{\rho_m}\Delta t\, Y(E,\theta) \tag{20}$$

where Δx is the erosion depth defined in the direction of the surface normal. While this equation can be easily applied to a planar surface, it is not obvious how to apply it to a cylindrical surface due to the change in the angle of incidence around the cylinder. Since finding an analytical solution for the erosion of a wire in the plume of a Hall effect thruster is difficult due to this curvature as well as the distribution of ion energies in the plume, the erosion is modeled by calculating how discretized, planar surfaces erode over time. An example discretization is shown in Fig. 5, where the ions are assumed to be traveling in negative y direction. A representative gold-molybdenum interface is also plotted for reference.

At a given time step, the angle of incidence of each surface in the cross section is calculated using the uniform

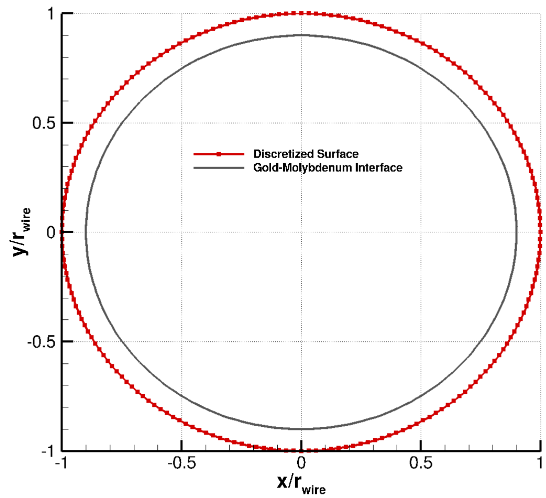

Fig. 5 Example discretization used in the erosion model. Gold-molybdenum interface not to scale.

incident ion direction and the normal to each surface. Since the wire is made of molybdenum coated with gold, each surface is determined to be either gold or molybdenum based on the distance of its midpoint from the cylinder axis, and the appropriate sputter yield model for each material is used. Assuming singly-charged ions, the total sputter yield is determined by summing the contributions of the sputter yield of each ion energy present in the IEDF

$$Y(E,\theta) = \sum_{i=0}^{N} Y(E_i,\theta) f(E_i) \tag{21}$$

The IEDFs are normalized such that $\sum_{i=0}^{N} f(E_i) = 1$. Using the total sputter yield, the erosion depth of each surface is calculated, and the endpoints of the surfaces are moved as shown in Fig. 6. First, the position the endpoint (x, y) would move to based on the erosion depth of each adjacent surface is calculated. In Fig. 6, these points are $(x_{n,1}, y_{n,1})$ and $(x_{n,2}, y_{n,2})$. The endpoint is then moved to the average x and y values of those two points, or $(x_n, y_n) = (\frac{x_{n,1}+x_{n,2}}{2}, \frac{y_{n,1}+y_{n,2}}{2})$. This process is repeated through the time steps until the total time is reached, the wire has totally eroded, or no additional erosion occurs.

If a surface is shielded from the incident ion direction, the erosion depth of that surface is set to zero because no ions impact the surface. Additionally, if an endpoint is shielded from the incident ion direction, that endpoint is not moved. Endpoints can be reset if a peak forms in the wire profile. A schematic showing how the endpoints are reset is shown in Fig. 7a for negative values of x, and a similar process holds for positive values of x. In this figure, the surface between (x_1, y_1) and (x_2, y_2) erodes, and those endpoints are moved to $(x_{n,1}, y_{n,1})$ and $(x_{n,2}, y_{n,2})$. If $|x_{n,2}|$ is larger than $|x_3|$, $(x_{n,2}, y_{n,2})$ is reset to the intersection of the surfaces formed by $(x_{n,1}, y_{n,1})$ and $(x_{n,2}, y_{n,2})$ and by (x_2, y_2) and (x_3, y_3). Unphysical loops can form when large amounts of erosion occur. The model determines when these loops form by detecting when two non-adjacent surfaces intersect. To resolve these unphysical loops, one point involved in the loop is reset to the intersection of those surfaces, and all others are deleted from the model, as shown schematically in Fig. 7b. Endpoints can also be deleted when their distance from the cylinder axis is larger than the specified wire radius.

III. Results

Experimental measurements of the plume properties and eroded wire profiles are compared to the model results. Experimental testing of the erosion of a meshed reflector was conducted at the Large Vacuum Test Facility at the University of Michigan with the H6US thruster. This thruster has been studied extensively, as shown in [16–18]. The first stage of experimental testing measured plume properties including the ion current density and IEDF along an arc at 1 m from the thruster. These results were compared to the results of MPIC. The second stage of experimental testing placed samples of the meshed reflector at 1 m from the thruster and various angles from the thruster centerline. The

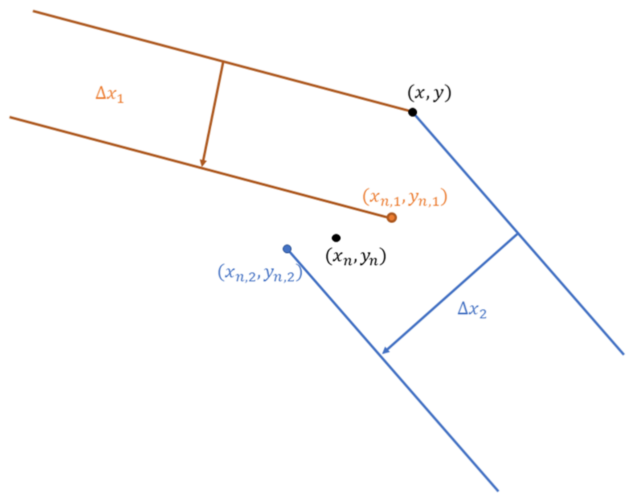

Fig. 6 Process for moving endpoints. The endpoint (x, y) is moved to $(x_n, y_n) = (\frac{x_{n,1}+x_{n,2}}{2}, \frac{y_{n,1}+y_{n,2}}{2})$.

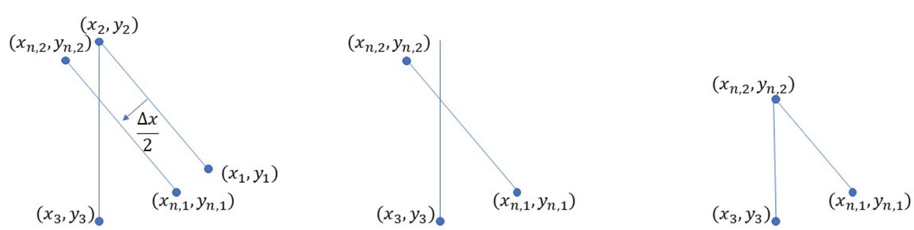

(a) Process for resetting points. Since $|x_{n,2}| > |x_3|$, $(x_{n,2}, y_{n,2})$ is reset to the intersection of the surfaces.

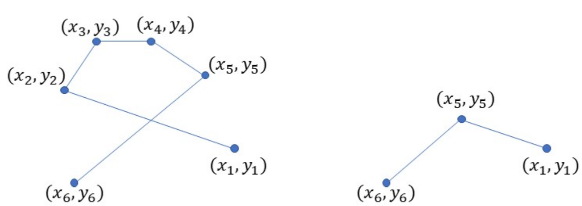

(b) Process for deleting points. In the loop, (x_5, y_5) is reset to the intersection of the surfaces, and all other points are deleted.

Fig. 7 Schematics of when points can be reset and deleted.

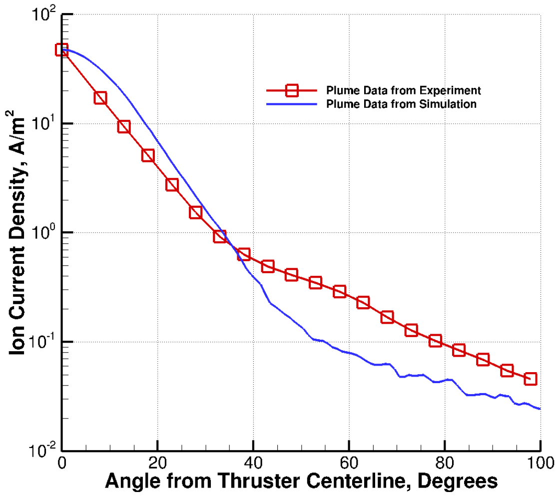

Fig. 8 Ion current density at 1 m from the thruster exit.

samples were exposed to the plume of the thruster for 10 hours. After experimental testing was completed, wires of the meshed reflectors were measured by optical profilometry at five different locations on the wire to obtain height profiles. More details on the experimental testing can be found in Part 2 of this work in [5].

This section first compares the experimentally measured plume properties to the results of MPIC. Then, results of the erosion model are presented. Results at 18°, 33°, 48°, and 63° from the thruster centerline are examined. These locations are chosen because they have very different plume properties, so a variety of eroded wire profiles are achieved. Therefore, plume properties were measured and meshed reflector samples were placed at these locations during the experimental testing.

A. Plume Modeling Results

The experimentally measured IEDFs are compared to the results of MPIC. The initial results of MPIC did not match the experimentally measured IEDFs well, especially at low angles from the thruster centerline. To better match the experimentally measured IEDFs at these low angles, the ion and neutral atom velocity and temperature at the effective inlet were adjusted.

Figure 9 shows the IEDFs at 18°, 33°, 48°, and 63° from the thruster centerline that are used to model the erosion of a wire. The experimentally measured data and the simulation results after the boundary conditions were adjusted are shown in these figures. The experimentally measured IEDFs are an energy per charge distribution, while the results of MPIC are the IEDFs of only the singly charged ions. At 18° from the thruster centerline, the experimentally measured IEDF shows a peak near 280 eV. This peak is the energy of the ions in the beam from the thruster. The simulation accurately captures both the location and height of the peak in the IEDF. This peak is also seen at 33° and 48° from the thruster centerline, but it has a lower magnitude. A peak is seen at energies below 50 eV at 48° and 63° from the thruster centerline. This peak is due to CEX ions, and its location is predicted well by the simulation.

In addition to the IEDFs, the experimentally measured ion current density is compared to the ion current density from the simulation in Fig. 8. While the value of the ion current density on the thruster centerline is well predicted by the simulation, the simulation slightly overestimates the ion current density for angles less than 35° from the thruster centerline and underestimates the ion current density at larger angles from the thruster centerline.

While these IEDFs and ion current density agree qualitatively, the results are not exact. These discrepancies are influenced by various factors. An effective inlet along a magnetic field line in the near-field plume is used as the simulation does not account for magnetic field effects. The ion and neutral atom velocity and temperature at this inlet were initially derived from the results of another simulation HPHall, as discussed in [6]. These boundary conditions were then adjusted to match the operating condition of the thruster and to better match the experimentally measured IEDFs. Experimental measurements of the ion and neutral atom velocity and temperature at the effective inlet could

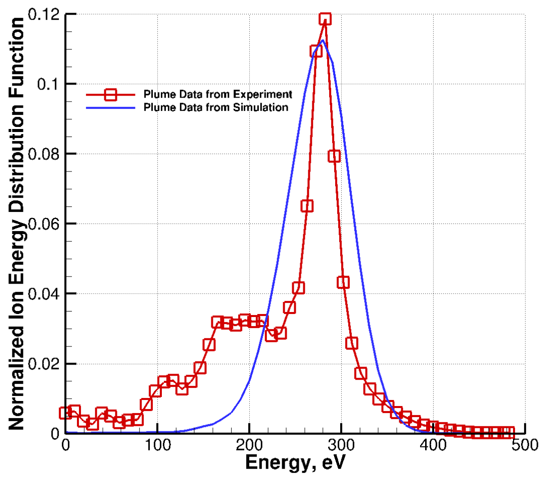

(a) 18° from the thruster centerline.

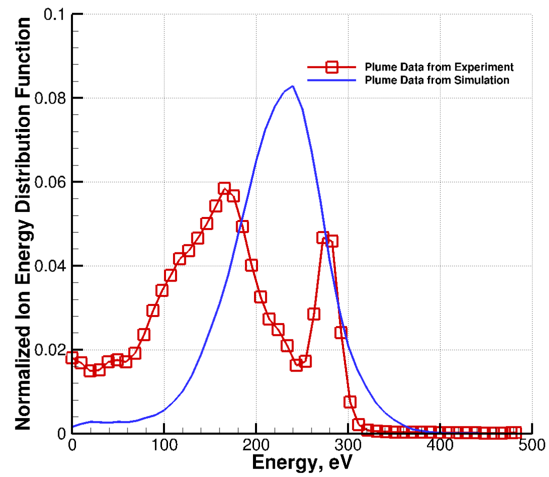

(b) 33° from the thruster centerline.

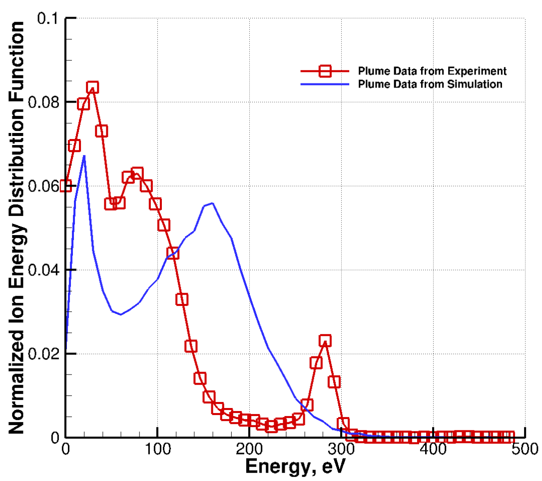

(c) 48° from the thruster centerline.

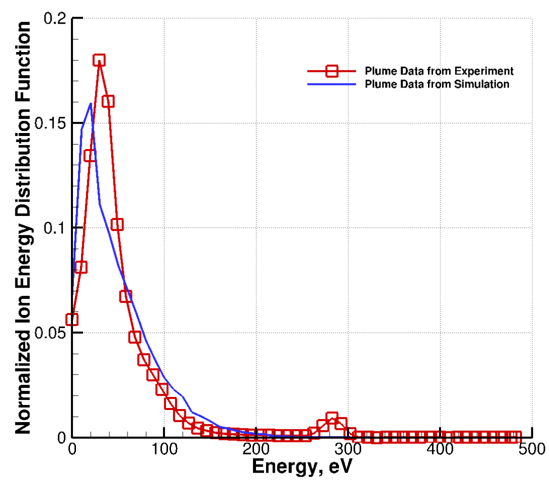

(d) 63° from the thruster centerline.

Fig. 9 IEDFs at 1 m from the thruster exit.

improve the agreement, as well as including magnetic field effects.

B. Wire Erosion Modeling Results

The erosion model is used to predict the profile of an eroded wire that is exposed to the plume for 10 hours at 18°, 33°, 48°, and 63° from the thruster centerline. The experimental measurements and simulation results provide the ion current density and IEDFs at those locations. First, the convergence of the erosion model with varying time steps is presented. Convergence of the model with varying numbers of initial surfaces is not considered in this work. Then, the results of the erosion model are compared to the experimentally measured wire profiles.

1. Convergence of the Model

The convergence of the model is assessed by varying the time step dt. To measure convergence, the profile after 10 hours of thruster operation is calculated for decreasing values of dt. Convergence is achieved when the difference between all endpoints that start at the same location is within 1% of the wire radius for two successive values of dt.

The erosion model results with different time steps are shown in Fig. 10 at 18°, 33°, 48°, and 63° from the thruster centerline using the Eckstein normal incidence model, the Wei angular incidence model, and experimentally measured plume properties. At 18° from the thruster centerline, the profiles converge at $dt = 0.05$ s. However, at the other three angles considered, the profiles converge at $dt = 10$ s. Results using other combinations of sputter yield models or the plume properties from the simulation at 18° from the thruster centerline converge at time steps as high as $dt = 0.5$ s or have yet to converge for time steps as low as $dt = 0.05$ s, and results at 33°, 48°, and 63° from the thruster centerline converge at $dt = 10$ s. As the size of the time step decreases, the erosion depth of each surface per time step decreases. Since the convergence depends on the erosion depth per time step, profiles at different angles from the thruster centerline converge at different time steps. At 18° from the thruster centerline, the erosion depth per time step is high due to the high current density and high energy of most of the ions. Therefore, the time step required to reach convergence is much smaller than the other angles from the thruster centerline.

2. Comparison to Experimentally Measured Profiles

The converged erosion model results or results with the lowest time step using the experimental measurements and simulation plume properties can be compared to the experimentally measured profiles. These profiles were measured at five different points along the wire and are averaged by x value to give one profile with error bars corresponding to the standard deviation. Since the experimentally measured wire profiles were measured with a profilometer, the exact height is not known. The experimentally measured profiles are then placed at heights that most closely match the erosion model results in each figure. Figs. 11, 12, 13, and 14 show the erosion model results with the plume properties from experiment and simulation at 18°, 33°, 48°, and 63° from the thruster centerline with different combinations of normal and angular incidence sputter yield models.

Most of the erosion model results using the plume properties from simulation at 18° from the thruster centerline predict significantly more erosion than the results using the plume properties from experiment and the experimentally measured profiles. The amount of erosion is overestimated because of the difference in the plume properties predicted by the simulation and measured experimentally at this location. The ion current density is higher in the simulation results than in the experimental measurements, and the IEDF in the simulation results predicts more ions will have a higher energy than in the experimental measurements. This difference in the IEDF leads to an increase in the sputter yield when the plume properties from the simulation are used. One combination of sputter yield models predicts less erosion near $\frac{x}{r_{wire}} = 0$ when using the plume properties from simulation than the experimentally measured profiles show, as seen in Fig. 11d. This difference is due to the dependence of the fit parameters of the Yamamura angular incidence model for molybdenum on threshold energy as illustrated in Fig. 4b by the profiles at 250 eV. Since the Yamamura angular incidence model with the threshold energy of the Bohdansky formula predicts more sputtering at the optimal angle than the model with the threshold energy of the Eckstein normal incidence model at its optimal angle, the decrease of the sputter yield to zero is faster for the model with the threshold energy of the Bohdansky formula than the decrease of the model with the threshold energy of the Eckstein normal incidence model. Peaks are able to form at larger y values due to the sputter yield decreasing to zero more quickly. The difference in the results using the simulation data in Figs. 11a and 11b is explained by the differing sputter yield predicted by the normal incidence sputter yield models for gold. At energies above 200 eV, the Ikuse normal incidence model predicts more sputtering than the Eckstein normal incidence model. Therefore, the gold layer erodes away faster when the Ikuse normal incidence model

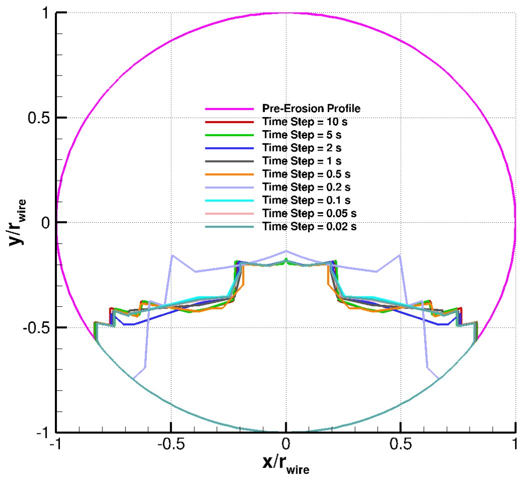

(a) 18° from the thruster centerline.

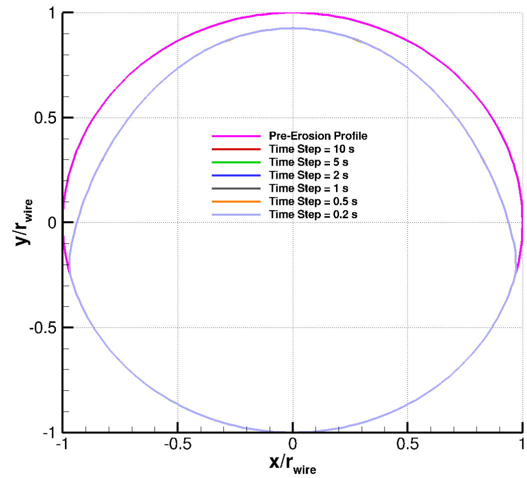

(b) 33° from the thruster centerline.

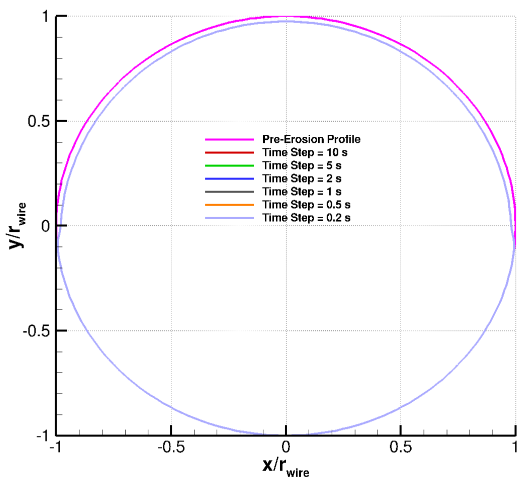

(c) 48° from the thruster centerline.

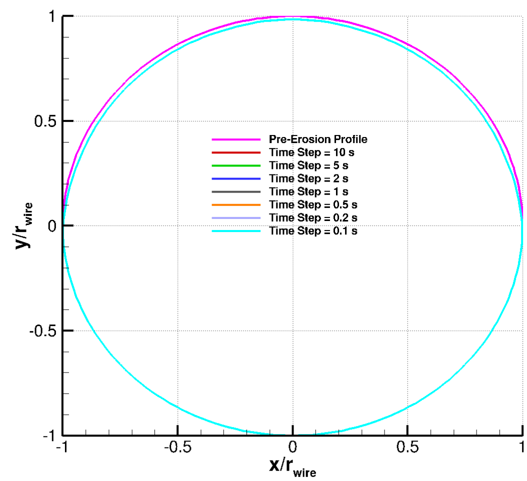

(d) 63° from the thruster centerline.

Fig. 10 Convergence of the model with the Eckstein normal incidence model and the Wei angular incidence model for both gold and molybdenum. Plume properties from experimental measurements.

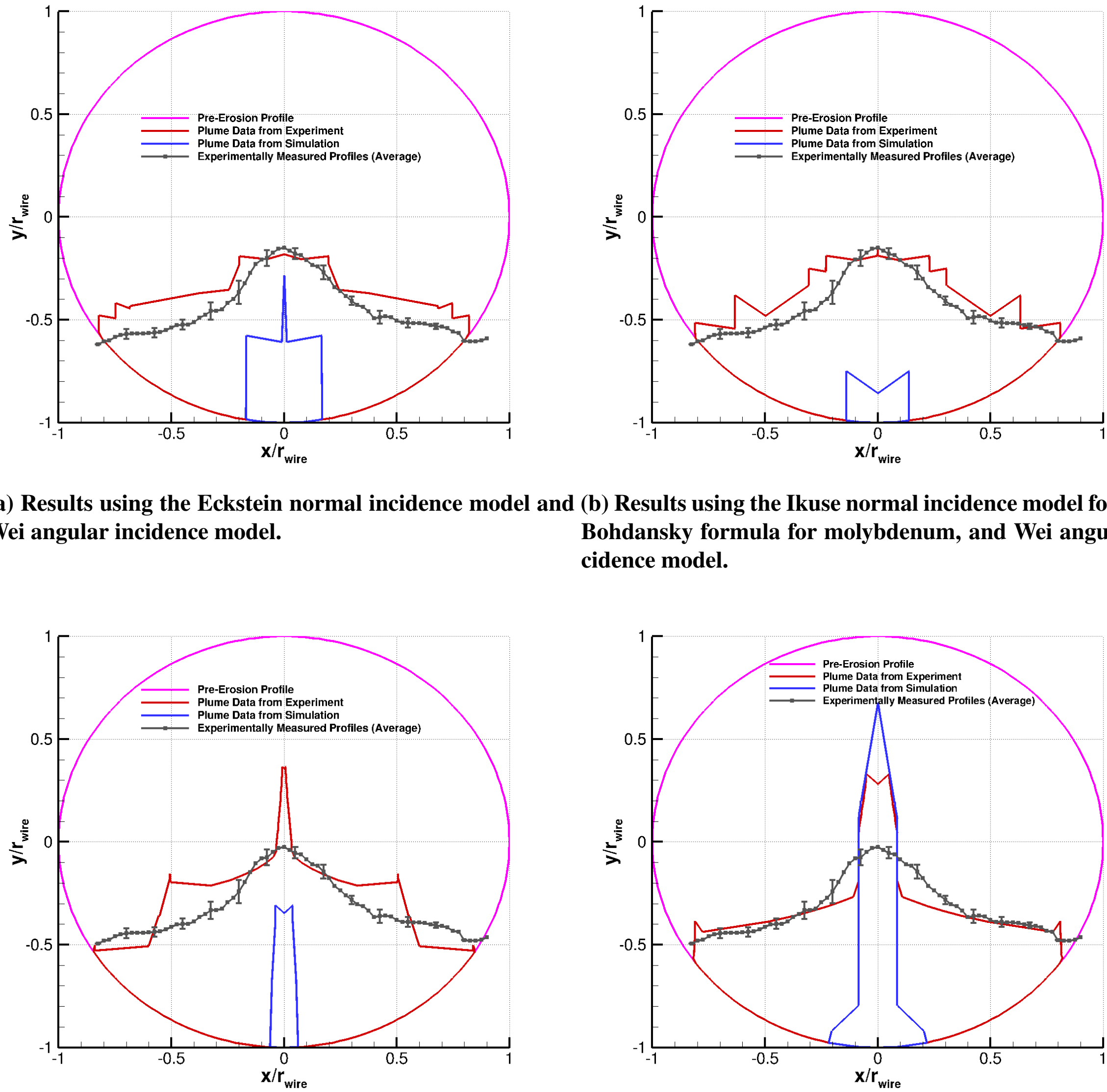

(a) Results using the Eckstein normal incidence model and Wei angular incidence model.

(b) Results using the Ikuse normal incidence model for gold, Bohdansky formula for molybdenum, and Wei angular incidence model.

(c) Results using the Eckstein normal incidence model and Yamamura angular incidence model.

(d) Results using the Ikuse normal incidence model for gold, Bohdansky formula for molybdenum, and Yamamura angular incidence model.

Fig. 11 Comparison of the erosion model results and experimentally measured profiles at 18° from the thruster centerline.

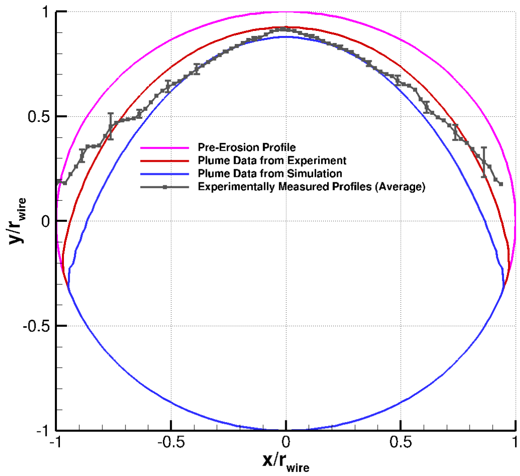

(a) Results using the Eckstein normal incidence model and Wei angular incidence model.

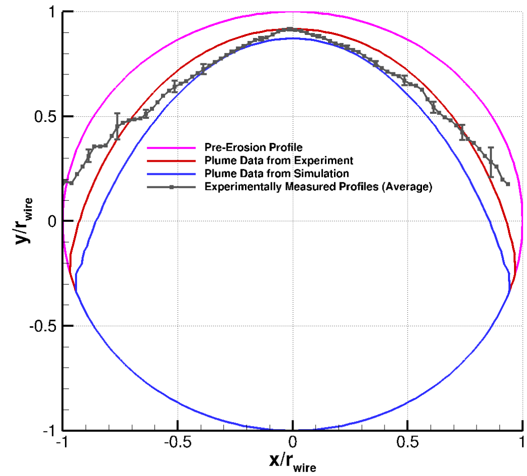

(b) Results using the Ikuse normal incidence model for gold, Bohdansky formula for molybdenum, and Wei angular incidence model.

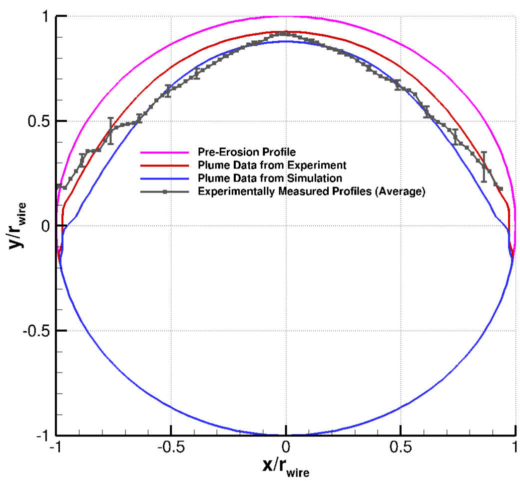

(c) Results using the Eckstein normal incidence model and Yamamura angular incidence model.

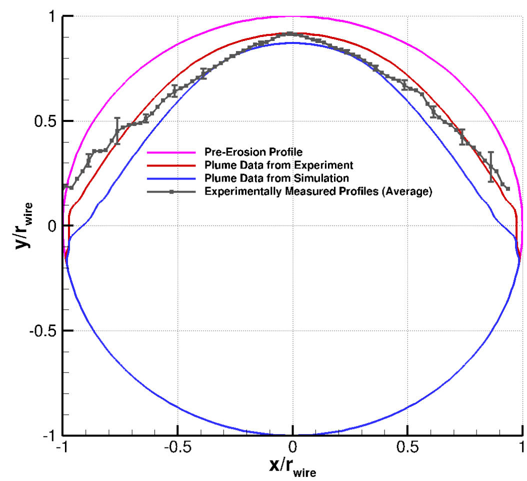

(d) Results using the Ikuse normal incidence model for gold, Bohdansky formula for molybdenum, and Yamamura angular incidence model.

Fig. 12 Comparison of the erosion model results and experimentally measured profiles at 33° from the thruster centerline.

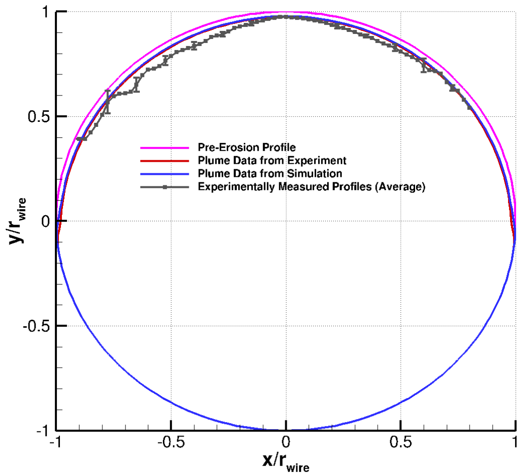

(a) Results using the Eckstein normal incidence model and Wei angular incidence model.

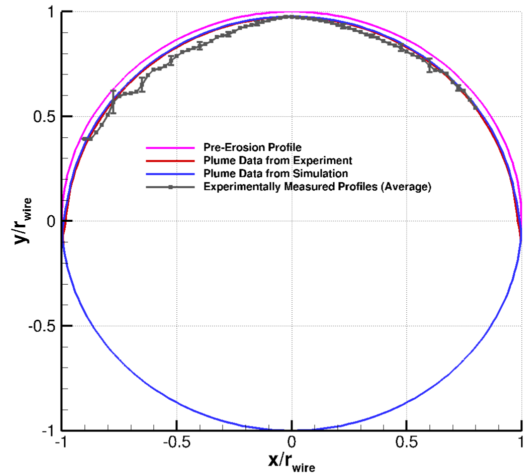

(b) Results using the Ikuse normal incidence model for gold, Bohdansky formula for molybdenum, and Wei angular incidence model.

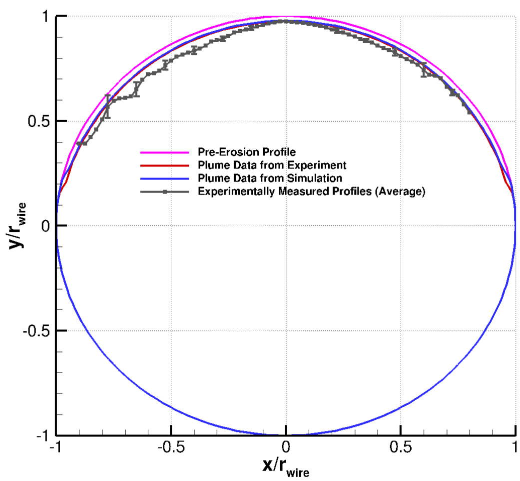

(c) Results using the Eckstein normal incidence model and Yamamura angular incidence model.

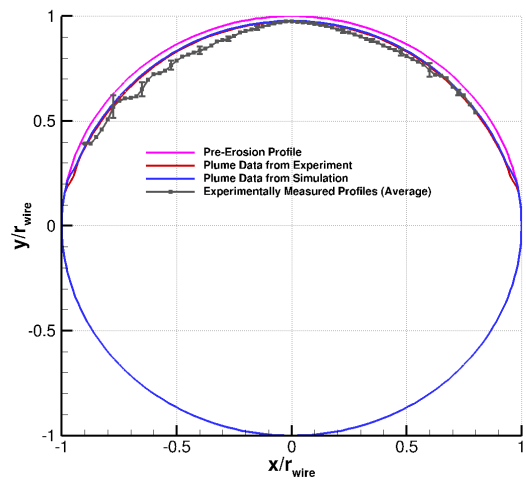

(d) Results using the Ikuse normal incidence model for gold, Bohdansky formula for molybdenum, and Yamamura angular incidence model.

Fig. 13 Comparison of the erosion model results and experimentally measured profiles at 48° from the thruster centerline.

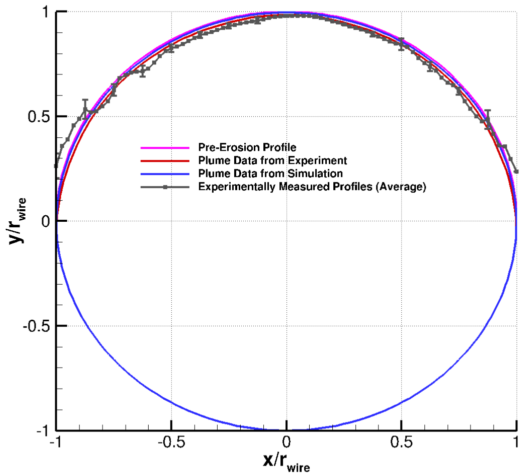

(a) Results using the Eckstein normal incidence model and Wei angular incidence model.

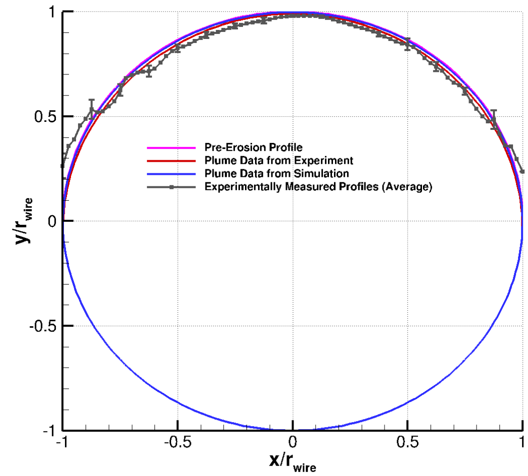

(b) Results using the Ikuse normal incidence model for gold, Bohdansky formula for molybdenum, and Wei angular incidence model.

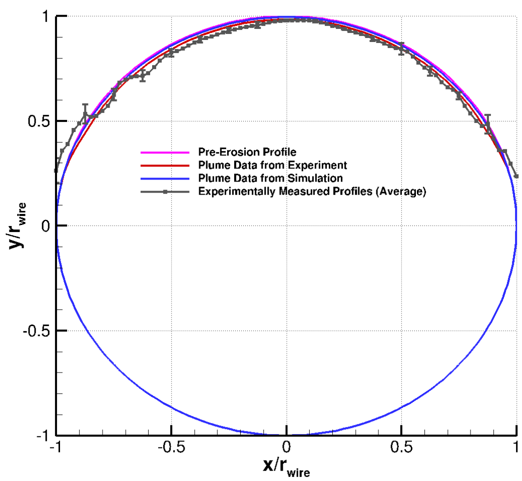

(c) Results using the Eckstein normal incidence model and Yamamura angular incidence model.

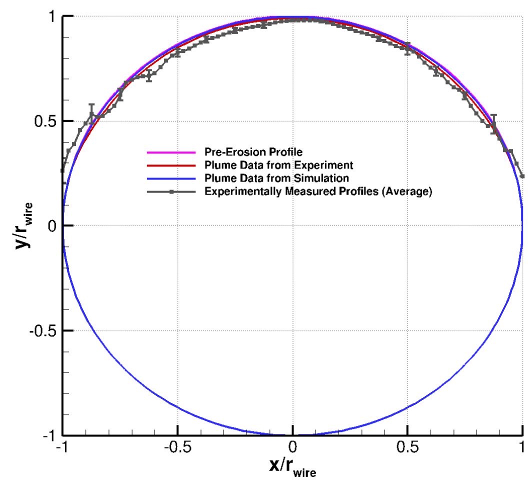

(d) Results using the Ikuse normal incidence model for gold, Bohdansky formula for molybdenum, and Yamamura angular incidence model.

Fig. 14 Comparison of the erosion model results and experimentally measured profiles at 63° from the thruster centerline.

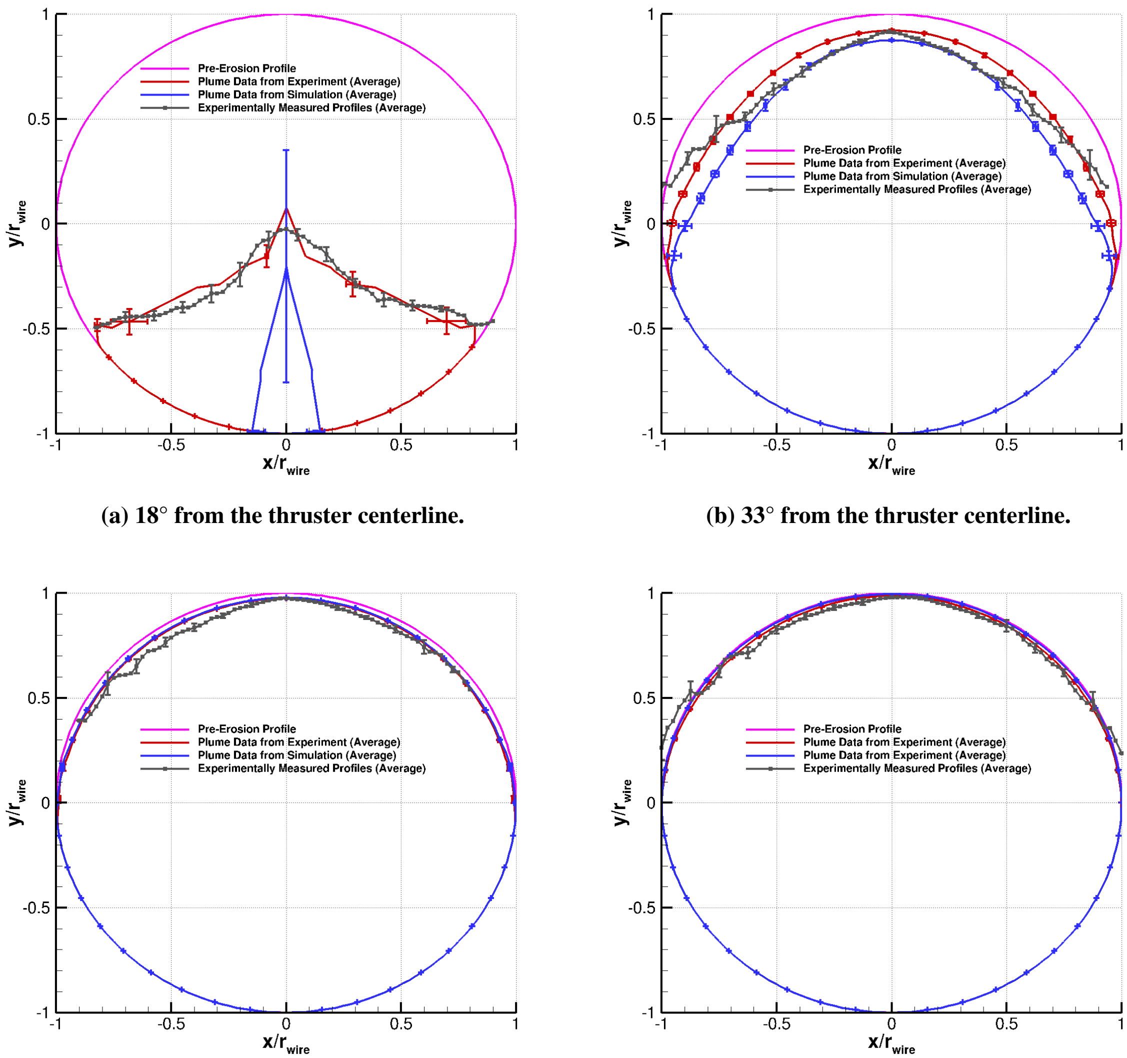

(a) 18° from the thruster centerline.

(b) 33° from the thruster centerline.

(c) 48° from the thruster centerline.

(d) 63° from the thruster centerline.

Fig. 15 Comparison of the average of the erosion model results and experimentally measured profiles.

is used. Since the gold layer coats the wire, this difference in the sputter yields affects the profile even when a large amount of erosion has occurred. The results using the experimentally measured plume properties and the Yamamura angular incidence sputter yield model at 18° from the thruster centerline predict a taller peak than the results using the Wei angular incidence model. This taller peak forms because the Yamamura angular incidence model predicts the sputter yield rapidly decreases to zero at angles of incidence beyond the optimal angle, as shown previously in Fig. 4a. Therefore, very little erosion of surfaces with large angles of incidence occurs. Since the Wei angular incidence model does not approach zero as quickly as the Yamamura angular incidence model, the tall peak is not seen in the profiles using the Wei angular incidence model. The results at 18° from the thruster centerline using the experimentally measured plume properties and the Wei angular incidence sputter yield model capture the height of the peak of the experimentally measured profiles. The small, jagged features in the results form because adjacent surfaces have different angles of incidence, which leads to different amounts of erosion of each surface.

At 33° from the thruster centerline, the erosion model results using the plume properties from the simulation predict more erosion than the results using the experimentally measured plume properties. This overestimation is again due to the ion current density from the simulation results being higher than the experimentally measured ion current density. While all results shown in Fig. 12 predict the erosion near $\frac{x}{r_{wire}} = 0$ well, the Yamamura angular incidence model with the experimental dataset best captures the erosion depth near $\frac{x}{r_{wire}} = \pm 1$. This is because the Yamamura model predicts low sputter yields at angles of incidence beyond the optimal angle. The erosion model results at 48° and 63° from the thruster centerline predict a small amount of erosion. The differences between the predictions using different datasets or different sputter yield models are not significant. All results at these angles predict the experimentally measured profiles well.

At each location in the plume, the erosion model results using the four different combinations of sputter yield models can be averaged to produce an average profile. The average is calculated by first determining the angle between the line segment from $(0, -r_{wire})$ to each endpoint in the profile from the line $y = -r$. The endpoints with the closest angle are then averaged. The average profiles using the plume properties from experiment and simulation are shown in Fig. 15, with error bars corresponding to the standard deviation. At 18° from the thruster centerline, the averaged profile using the plume properties from simulation again overestimates the amount of erosion. The averaged profile using the plume properties from experiment matches the experimentally measured profile relatively well, as the endpoints in the average profile agree with the measured points with the closest x value to within 20% of a wire radius. The tall peak seen previously in the profiles using the Yamamura angular incidence model has been reduced because the profiles using the Wei angular incidence model do not have that feature. At 33° from the thruster centerline, both averaged profiles capture the erosion near $\frac{x}{r_{wire}} = 0$. However, neither averaged profile accurately captures the profile near $\frac{x}{r_{wire}} = \pm 1$ because the sputter yield predicted by the Wei angular incidence model does not decrease to zero as rapidly as the sputter yield predicted by the Yamamura angular incidence model does, leading to more erosion at large angles of incidence. The averaged result using the experimentally measured plume properties agrees with the average measured profile to within 35% of a wire radius, with the differences more than 20% of the wire radius near $\frac{x}{r_{wire}} = -1$. At 48° and 63° from the thruster centerline, the averaged profiles predict the experimentally measured data relatively well. Differences between the average measured profile are within 20% of the wire radius at all endpoints except near $\frac{x}{r_{wire}} = \pm 1$.

While the erosion model results using the plume properties from experiment best predict the experimentally measured wire profiles, the results using the simulated plume properties give a good estimate of the erosion. This estimate captures the experimentally measured profiles relatively well at 33°, 48°, and 63° from the thruster centerline. While the erosion at 18° from the thruster centerline is not accurately captured by results using the plume properties from simulation, the results using the simulated plume properties still predict that the wire will be significantly eroded. Therefore, the erosion model can be used with simulated plume properties to estimate the erosion of a wire in the plume of EP devices if experimentally measured properties are not available.

IV. Discussion

Because the erosion of a wire differs from the erosion of a planar surface due to the change in angle of incidence around the wire, estimates of erosion of meshed reflectors assuming these reflectors are planar surfaces can underestimate the erosion experienced by the reflector. The erosion depth of a flat molybdenum surface coated with gold is shown in Fig. 16 after being exposed to the plume for 10 hours. This erosion depth is calculated using the Eckstein normal incidence model, the Wei angular incidence model, and the experimentally measured plume properties at 18° from the thruster centerline. The maximum modeled erosion depth on a wire after being exposed to the plume for the same amount of time is also shown using the same sputter yield models and plume properties. At angles of incidence near

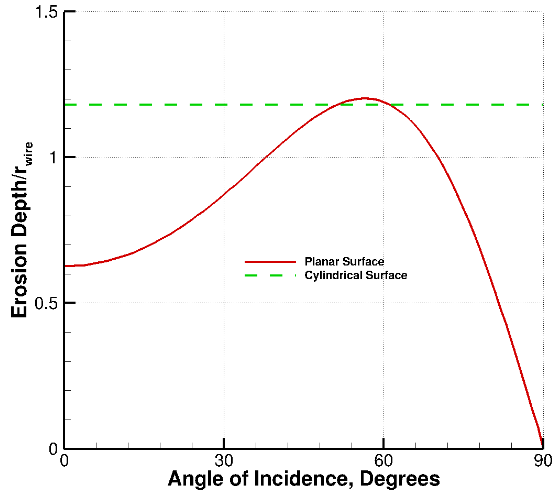

Fig. 16 Erosion depth of a planar surface for different angles of incidence. The maximum erosion depth on a wire is plotted for reference.

the optimal angle of the Wei angular incidence model for molybdenum, the erosion depth assuming a planar surface matches the maximum erosion depth on a wire. However, at angles of incidence above or below the optimal angle, the erosion depth assuming a planar surface is much less than the maximum erosion depth on a wire under the same conditions. Since significant amounts of erosion can damage the meshed reflector, underestimating the erosion can lead to unexpected decreased performance or failure of the meshed reflector.

Averaging the erosion model results with different sputter yield models produces better agreement with the experimentally measured profiles than considering one combination of sputter yield models. While the Yamamura and Wei angular incidence sputter yield models predict different sputter yields at various angles of incidence, these differences are averaged out when the average of the profiles is taken, as seen in Fig. 15a. The averaging can also reduce the uncertainties associated with the sputter yield models. While the fit parameters of the sputter yield models have an uncertainty, using two different sputter yield models and averaging those results can better estimate the actual sputter yield.

There are many limitations of the erosion model. The sputter yield models used in this paper do not necessarily represent the experimentally measured sputter yields accurately, and the sputter yields are difficult to measure due to the many factors including surface roughness that influence the values[3]. To overcome this limitation, the fit parameters of the sputter yield models can be assumed to be normally distributed, with a mean and maximum likelihood value as discussed by Yim in [3] for the Eckstein normal incidence model and the Wei angular incidence model. The erosion model then randomly draws values for the fit parameters from the normal distribution and calculates the eroded wire profile. Using many profiles, an average profile with confidence intervals of erosion can be determined.

The erosion model can also be improved by considering additional plume properties. The model currently assumes all of the ions are incident on the wire from a uniform direction. While this assumption may hold at low angles from the thruster centerline in the beam of ions from the thruster, it may not hold outside of the beam where the motion of CEX ions is influenced primarily by the local electric field. The various directions of the incident ions is captured by the ion velocity distribution function in three dimensions. The effects of multiply-charged ions can also be incorporated into the erosion model. The erosion model assumes that the ions are all singly-charged; however, as shown in Part 2 of this work, about 15% of the ions are multiply-charged in the H6 plume. Multiply-charged ions typically have a higher energy than singly-charged ions, and since the sputter yield is nonlinear in ion energy, multiply-charged ions can affect the sputter yield and the erosion.

V. Conclusion

EP devices used on satellites can affect many components of the satellite, including meshed reflectors that are composed of small wires. This study detailed the development of a model to predict the eroded profile of a single wire exposed to the plume of an EP device. The model discretized the cross section of a wire into planar surfaces and calculated how those surfaces erode through time. The erosion model required the IEDF and the ion current density at the location of the wire in the plume to calculate the erosion depth of each discretized surface. These parameters were either determined by a plume simulation or measured experimentally.

Experimental testing was conducted at the University of Michigan to measure the plume properties and the eroded wire profiles, which is detailed in Part 2 of this work[5]. The results of the experimental testing were compared to the results of the plume simulation MPIC and to the results of erosion model. Using different normal and angular incidence sputter yield models in the erosion model produced different profiles. The differences between these sputter yield models were especially prominent in the profile at 18° from the thruster centerline, where a large amount of erosion occurs in 10 hours. The profiles with different sputter yield models were averaged at each location in the plume, and these averaged profiles provided good agreement with the experimentally measured profiles.

While the experimentally measured plume properties best predict the experimentally measured profiles, the plume properties from the simulation predicted the amount of erosion relatively well, especially at large angles from the thruster centerline. Therefore, the erosion model can be used to predict the erosion of a wire in the plume of other electric propulsion devices, even if the experimentally measured ion current density and IEDFs are not available. This prediction is valuable as the amount of erosion can affect the performance of meshed reflectors.

Acknowledgments

The authors would like to acknowledge the following funding sources: Rackham Merit Fellowship, Plasmadynamics and Electric Propulsion Laboratory, and the Applied Physics Program.

References

[1] Oh, D. Y., Hastings, D. E., Marrese, C. M., Haas, J. M., and Gallimore, A. D., "Modeling of Stationary Plasma Thruster-100 Thruster Plumes and Implications for Satellite Design," *Journal of Propulsion and Power*, Vol. 15, No. 2, 1999, pp. 345–347. doi:10.2514/2.5432.

[2] Boyd, I. D., and Falk, M. L., "A review of spacecraft material sputtering by Hall thruster plumes," *AIAA 37th Joint Propulsion Conference*, American Institute of Aeronautics and Astronautics, Salt Lake City, UT, 2001.

[3] Yim, J. T., "A survey of xenon ion sputter yield data and fits relevant to electric propulsion spacecraft integration," *35th International Electric Propulsion Conference*, Atlanta, GA, 2017.

[4] Rubin, B., Topper, J. L., Farnell, C. C., and Yalin, A. P., "Quartz crystal microbalance-based system for high-sensitivity differential sputter yield measurements," *Review of Scientific Instruments*, Vol. 80, No. 10, 2009, pp. 103506–103506–9. doi:10.1063/1.3249560.

[5] Byrne, M. P., Meyer, M. E., Boyd, I. D., and Jorns, B. A., "Erosion of a meshed reflector in the plume of a Hall effect thruster, Part 2: Experiments," *AIAA Propulsion and Energy Forum and Exposition*, 2019. Submitted for publication.

[6] Huismann, T. D., "Improving Hall Thruster Plume Simulation through Refined Characterization of Near-field Plasma Properties," Ph.D. thesis, University of Michigan Ann Arbor, 2011.

[7] Boyd, I. D., and Yim, J. T., "Modeling of the near field plume of a Hall thruster," *Journal of Applied Physics*, Vol. 95, No. 9, 2004, pp. 4575–4584. doi:10.1063/1.1688444.

[8] Ahedo, E., Martínez-Cerezo, P., and Martínez-Sánchez, M., "One-dimensional model of the plasma flow in a Hall thruster," *Physics of Plasmas*, Vol. 8, No. 6, 2001, pp. 3058–3068. doi:10.1063/1.1371519.

[9] Bohdansky, J., "A universal relation for the sputtering yield of monatomic solids at normal ion incidence," *Nuclear Instruments and Methods in Physics Research, B*, Vol. 2, No. 1, 1984, pp. 587–591. doi:10.1016/0168-583X(84)90271-4.

[10] García-Rosales, C., Eckstein, W., and Roth, J., "Revised formulae for sputtering data," *Journal of Nuclear Materials*, Vol. 218, No. 1, 1995, pp. 8–17. doi:10.1016/0022-3115(94)00376-9.

[11] Tartz, M., Heyn, T., Bundesmann, C., Zimmermann, C., and Neumann, H., "Sputter yields of Mo, Ti, W, Al, Ag under xenon ion incidence," *The European Physical Journal D*, Vol. 61, No. 3, 2011, pp. 587–592. doi:10.1140/epjd/e2010-10553-8.

[12] Ikuse, K., Yoshimura, S., Hine, K., Kiuchi, M., and Hamaguchi, S., "Sputtering yields of Au by low-energy noble gas ion bombardment," *Journal of Physics D: Applied Physics*, Vol. 42, No. 13, 2009. doi:10.1088/0022-3727/42/13/135203.

[13] Eckstein, W., and Preuss, R., "New fit formulae for the sputtering yield," *Journal of Nuclear Materials*, Vol. 320, No. 3, 2003, pp. 209–213. doi:10.1016/S0022-3115(03)00192-2.

[14] Yamamura, Y., and Shindo, S., "An empirical formula for angular dependence of sputtering yields," *Radiation Effects*, Vol. 80, No. 1-2, 1984, pp. 57–72. doi:10.1080/00337578408222489.

[15] Wei, Q., Li, K.-D., Lian, J., and Wang, L., "Angular dependence of sputtering yield of amorphous and polycrystalline materials," *Journal of Physics D: Applied Physics*, Vol. 41, No. 17, 2008, p. 172002. doi:10.1088/0022-3727/41/17/172002.

[16] Brown, D. L., "Investigation of low discharge voltage Hall thruster characteristics and evaluation of loss mechanisms," Ph.D. thesis, University of Michigan Ann Arbor, 2009.

[17] Reid, B. M., "The influence of neutral flow rate in operation of Hall thrusters," Ph.D. thesis, University of Michigan Ann Arbor, 2009.

[18] Shastry, R., "Experimental Characterization of the Near-Wall Region in Hall Thrusters and its Implications on Performance and Lifetime," Ph.D. thesis, University of Michigan Ann Arbor, 2011.